


# Enhanced Sensitivity of Subwavelength Multibox Waveguide Microring Resonator Label-Free Biosensors

Enxiao Luan , Han Yun, *Student Member, IEEE*, Loic Laplatine, Yonathan Dattner, Daniel M. Ratner, Karen C. Cheung, and Lukas Chrostowski, *Senior Member, IEEE*

(Invited Paper)

**Abstract**—In this paper, a novel silicon photonic waveguide for a high sensitivity label-free sensor is presented. We use silicon-on-insulator subwavelength waveguides that consist of five rows of periodic silicon squares with 60 nm gap distances between each square (multibox structure) to construct microring resonators to achieve higher bulk and surface sensitivities than the resonators using conventional strip waveguides. Due to the high surface contact area and low optical confinement of the proposed multibox waveguides, the sensitivity of the microring resonator can be significantly increased. By exposing the multibox microring resonators to ultrapure water and different concentrations of isopropyl alcohol solution, we show a bulk sensitivity of 579.5 nm/RIU, which is an increase compared to recently published subwavelength grating waveguides and strip waveguides in transverse magnetic polarization microring resonators. Finally, a standard biological sandwich assay is employed to demonstrate the multibox sensor's ability, with an enhanced surface sensitivity of 1900 pm/nm.

**Index Terms**—High sensitivity, sub-wavelength, multi-box, microring resonator, label-free biosensor.

## I. INTRODUCTION

**M**EDICAL diagnostics are critical in reducing treatment costs and improving outcomes by facilitating preventative care, early intervention, and targeted therapy. They affect 60–70% of all treatment decisions but only account for about

13% of all healthcare related costs [1]. Nowadays, the enzyme-linked immunosorbent assay (ELISA) is the gold-standard modern diagnostic tool with high sensitivity and accuracy [2], [3]. However, it suffers from expensive test costs (\$ 300–\$ 650) and a lengthy analysis time ( $\sim 1$ –3 hours) [1]. It also requires trained operators and secondary amplification steps with complex logistics and information management for data analysis [4], which restricts its adoption for fast in-field testing, especially in developing countries. As a result, developing ELISA-like, low-cost and simple-operating biosensors for lab-on-a-chip (LOC) applications has attracted much attention over the last decades.

Silicon photonics is an emerging technology that can be used to build large-scale photonic integrated circuits (PICs) for multiple functions into a single package. Most silicon PICs can be manufactured by mature fabrication facilities which offer a low cost for mass production [5]. Silicon photonic biosensors have attracted increasing attention due to their potential to be used for environmental monitoring, biothreat-associated agent detection, healthcare and basic biomedical research [4]. These optical biosensors use near-infrared light confined to silicon waveguides to sense the capture of molecules and particles on the surface of waveguides. The interaction between the evanescent fields, formed by a portion of the electric field traveling outside of the waveguide, and the surrounding volume creates a sensitive region to detect the waveguide effective index changes due to the change of the external refractive index (RI) over the surface [6]. Many silicon photonic biosensor systems choose resonant structures for detection, such as microring [7] and microdisk [8] resonators, Bragg gratings [9], and one-dimensional (1D) or two-dimensional (2D) photonic crystal microcavities [10]–[13]. In these structures, a tiny change in the external RI can cause a noticeable shift of the resonance frequencies and, thus, provide a measurable response. Moreover, silicon photonic biosensors are excellent transducers for continuous and quantitative label-free biosensing, due to their high manufacturability and compactness for simultaneous measurements on a single chip [14]. Although these optical structures have already shown clinically relevant sensitivities in nucleic acid detection [15], protein biomarkers for viral [16], cancer [17], and environmental poisons [18], many clinical diagnostic tests still require a lower detection limit [7], which is the motivation of this work.

Manuscript received December 2, 2017; revised February 16, 2018; accepted March 21, 2018. Date of publication April 4, 2018; date of current version June 8, 2018. This work was supported in part by the Natural Sciences and Engineering Research Council of Canada (NSERC), in part by the NSERC CREATE Silicon Electronic Photonic Integrated Circuits Research Training Program, in part by the MITACS Accelerate program, and in part by the Government of Canada's Business-Led Networks of Centres of Excellence Refined Manufacturing Acceleration Process program. Enxiao Luan received the support from the China Scholarship Council for four years study at the University of British Columbia. (Corresponding author: Enxiao Luan.)

E. Luan, H. Yun, L. Laplatine, K. C. Cheung, and L. Chrostowski are with the Department of Electrical and Computer Engineering, University of British Columbia, Vancouver, BC V6T 1Z4, Canada (e-mail: eluan@ece.ubc.ca; hany@ece.ubc.ca; laplatine@ece.ubc.ca; kcheung@ece.ubc.ca; lukasc@ece.ubc.ca).

Y. Dattner is with Luxmux Technology Corporation, Calgary, AB T1Y 7E5, Canada (e-mail: yonathan.dattner@luxmux.com).

D. M. Ratner is with the Department of Bioengineering, University of Washington, Seattle, WA 98195 USA (e-mail: dratner@uw.edu).

Color versions of one or more of the figures in this paper are available online at <http://ieeexplore.ieee.org>.

Digital Object Identifier 10.1109/JSTQE.2018.2821842

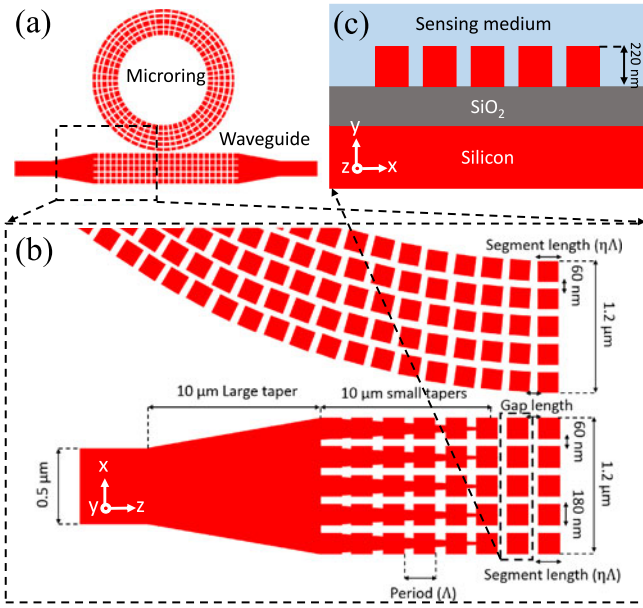


Fig. 1. (a) Schematic of a multi-box microring resonator and a multi-box coupling waveguide. (b) The magnified image of the black dashed box;  $\Lambda$  is the multi-box period, and the length of each Si segment is determined by the duty cycle  $\eta$ . (c) The magnified waveguide cross section showing the 5-row of multi-box segments with a thickness of 220 nm exposed in a sensing medium. The model is not in scale.

For common silicon photonic sensors, due to the high index contrast between the silicon core and the cladding, most of the electric field is confined in the core of the waveguide, which limits the overlap of the evanescent field and analyte. One method to enhance the electric field outside of the waveguide is to create a slot in the waveguide which leads to a large electric field in the slot and increases the interaction of the light with the material in the slot [19]. Another approach is to reduce the confinement of the silicon core by minimizing the index contrast, which has been demonstrated by sub-wavelength grating (SWG) waveguides [20]. A slot-waveguide device consists of two high index rails separated by a low index slot region, the double core structure acts as one waveguide [21]. The electric field intensity is mainly concentrated in the slot, which increases the field and analyte overlap and results in the bulk sensitivity of 212 nm/RIU [21] and 298 nm/RIU [22] in the transverse electric (TE) mode. Since the first demonstrations of an optical waveguide with an SWG metamaterial core at NRC Canada [23]–[25], SWG waveguides have attracted a strong research interest because of their unique potential to control light propagation in planar waveguides [26], [27]. The SWG structures decrease the effective index by replacing parts of the silicon core with a lower index material periodically, which releases more optical mode into the evanescent field, and increases the bulk sensitivity, e.g., 490 nm/RIU [28], 440.5 nm/RIU [29] in the TE mode, and 429.7 nm/RIU in the TM mode [30].

In this paper, we design an optimized silicon waveguide-based microring resonator that consists of five rows of  $180 \times 180 \text{ nm}^2$  periodic silicon squares with a gap of 60 nm and a thickness of 220 nm [see Fig. 1(b)]. Due to the gaps between the Si segments in both the transversal and propagation

directions, the effective refractive index of the optical mode is significantly reduced resulting in a less confined optical mode. The multi-box structure also enables more surface contact area around each Si segment for the analyte to attach. Thus, the sensitivity of the device using multi-box structures will be highly improved compared to SWG sensors. Based on the simulation results, a bulk sensitivity of 575.2 nm/RIU is achieved for the TE mode. Exposing the multi-box devices to IPA dilutions in ultrapure water at increasing concentrations gives us an experimental bulk sensitivity of 579.5 nm/RIU. The improvement factors compared to other microring resonators are 15X for the conventional TE mode waveguides (38 nm/RIU) [31], 1.18X for the SWG waveguides (490 nm/RIU) [28] and 2.3X for the TM strip waveguides microring resonators (250 nm/RIU) [32]. Finally, a standard bio-sandwich assay involving biomolecules with high binding affinities is selected to evaluate the surface biosensing performance of the multi-box microring resonator, and a surface sensitivity of 1900 pm/nm is observed, which is approximately 2X increase to an SWG microring resonator in the TE mode.

## II. THEORY AND SIMULATION RESULTS

Several numerical methods can be applied for the simulation of periodic waveguides [33]–[35]. The most rigorous is a full 3D vectorial Finite-Difference-Time-Domain (FDTD) approach, but for large and complicated structures this approach is time-consuming [28]. An alternative is to simulate a single unit cell using Bloch boundary conditions in the propagation direction, which has already been applied to simulate SWG and Bragg waveguides [28], [36]. By using this approach, an infinitely long multi-box waveguide can be studied effectively without considering the whole structure. For the simulations of the multi-box structure, FDTD Solutions from Lumerical Solutions, Inc. was employed.

### A. FDTD Analysis for the Effective Index

For conventional SOI silicon waveguides, the large refractive index contrast between the silicon core and the cladding layer leads to a strong confinement of the light propagating inside the waveguides. Since the multi-box waveguide has a relatively low effective index especially with water cladding ( $n_{\text{water}} = 1.32$  at  $\lambda = 1550 \text{ nm}$ ), this results in a weaker optical confinement with a large portion of the light propagating down in the substrate ( $n_{\text{sub}} = 1.44$  at  $\lambda = 1550 \text{ nm}$ ), giving rise to a leakage penalty. The leakage loss to the substrate is negligible when the thickness of the buried oxide (BOX) layer is higher than  $2 \mu\text{m}$  and the mode effective index is higher than 1.65, or when the thickness of the BOX layer is higher than  $3 \mu\text{m}$  and the mode effective index is higher than 1.55 [37]. To minimize the substrate leakage with a relatively low optical confinement, different numbers of multi-box rows with varied duty cycles in the propagation direction are considered to obtain a proper effective index. The gap between each segment is set to be 60 nm, which is the minimum feature size for our electron beam lithography process [38], and only the length of the Si parts is varied to change the duty cycle. We investigate our multi-box waveguides for both

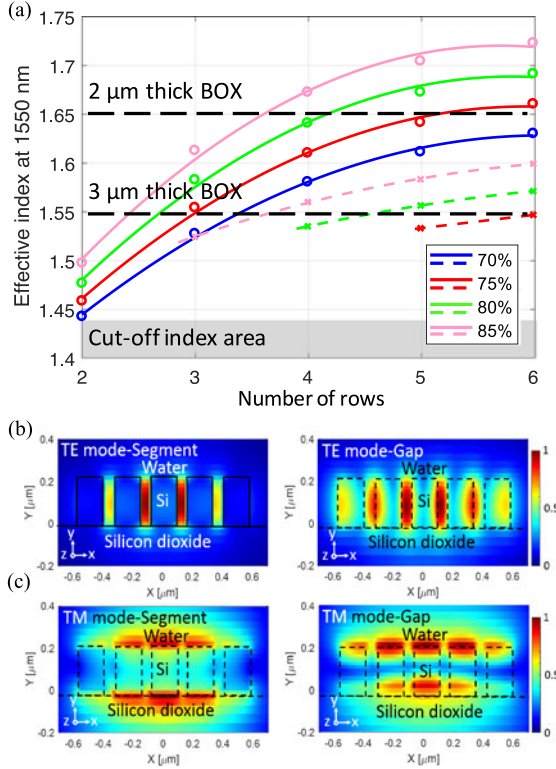


Fig. 2. (a) Simulated effective indices of multi-box waveguides with a varied number of rows and duty cycle for the single quasi-TE (dots) and quasi-TM (crosses) modes. The black dashed lines indicate the required refractive index for the negligible substrate leakage. The grey area shows the effective index value lower than the substrate. (b) Cross sections of the E field of Si segments and gaps in the TE. (c) TM modes with water cladding above in xy-plane ( $w = 1200$  nm,  $t = 220$  nm,  $\Lambda = 240$  nm and  $\eta = 75\%$ ).

the single quasi-TE and quasi-TM modes at 1550 nm. All the waveguides are with water cladding on top in our simulations. In Fig. 2(a), the multi-box structure shows a lower effective index in the TM mode (dashed lines) compared to that in the TE mode (solid lines), which is due to different electric field distributions presented in Fig. 2(b) and (c): most of the field intensity is congregated in the gaps in the TE mode, whereas, in the TM mode, the field distribution is similar to the conventional strip waveguide, above and beneath the Si core, which may not achieve a higher sensing performance than a conventional strip waveguide operated in the TM mode. There is a cut-off index region presented in Fig. 2(a), where the effective index value is lower than the RI of the substrate resulting in no guided mode. To have a higher surface contact area with a low substrate leakage, the multi-box structure with five rows and 75% duty cycle in the TE mode is considered as the basic geometry of the multi-box microring resonator with a simulated group index of 2.15 at  $\lambda = 1550$  nm.

### B. Loss

All the waveguides are designed to have their periods much smaller than the Bragg condition, i.e.,  $\Lambda \ll \lambda/(2n_{\text{eff}})$ . Therefore the periodic waveguide structures support lossless Floquet-Bloch (FB) modes [39]. However, even though the SWG

waveguides theoretically support modes much like conventional strip waveguides, there are excess loss mechanisms. Due to the low optical confinement of the multi-box structure, a variety of loss mechanisms occur when light propagates along the waveguides, such as substrate leakage loss, mode mismatch losses, bend radiation losses, sidewall roughness-induced scattering losses and material absorption. Mode mismatch is caused by the imperfect mode overlap between different waveguide geometries, like the straight and the bent waveguides, and the strip and the multi-box waveguides, which leads to scattering at the abruptly transformed regions [5]. Scattering losses are associated with the coupling of the forward-propagating modes with radiation modes as well as with the backward-propagating modes (back-scattering) [40]. Material absorption, especially caused by the water cladding, is the primary optical loss for silicon photonic biosensors at a wavelength of 1550 nm (the optical absorption of water is 42.5 dB/cm), since many analytes of interest are found in aqueous solutions. For the conventional strip waveguides in the TE mode, the propagation loss is around 4 dB/cm, which mainly originates from scattering due to the surface roughness [41]. For multi-box waveguides, the outer sidewall interaction is reduced due to the gaps between the segments in the propagation direction, and the mode delocalization. However, the roughness of the multiplied internal sidewalls and a low effective index should be considered, thus a precise loss analysis remains to be carried out as has been done for various other waveguides and photonic crystals [40].

Fig. 3(a) presents the simulated propagation loss in the 5-row multi-box waveguides ( $w = 1200$  nm,  $t = 220$  nm,  $\Lambda = 240$  nm and  $\eta = 75\%$ ) with a varied length using 3D-FDTD simulations of a finite length waveguide. All the devices are simulated above a 2-μm-thick BOX layer in the TE mode at 1550 nm with water cladding on top. By increasing the length of the multi-box waveguides from 10 to 60 μm, a linear-fitted curve of the propagation loss of 27.56 dB/cm is obtained which is mainly generated from the water absorption.

To have a small footprint for silicon photonic biosensors that use microring resonators with high quality factors, the waveguide bend loss need to be studied. It has been reported that the bend loss is negligible at a radius of approximately 10 μm for a conventional strip waveguide [42]. By increasing the bend radius, the bend loss can be reduced to the point where it equals the waveguide propagation loss [5]. To ensure low bend loss with a small footprint, we model the bend loss with varied radius by 3D-FDTD simulations. The waveguide bend loss with water cladding versus radius is observed and plotted in Fig. 3(b) in both dB and log dB scales. Moreover, on the plots, a dashed line is included for the propagation loss in water. For the multi-box bend with a radius larger than 30 μm, the loss per bend including water absorption and bend radiation has been reduced to  $9 \times 10^{-2}$  dB [see the inset of Fig. 3(b)].

According to the research from Baehr-Jones *et al.* [43], the scattering loss of a slot waveguide is around 8 to 10 dB/cm, more than a conventional strip waveguide. Hence for the multi-box waveguide, additional scattering loss caused by the sidewall roughness is not negligible due to its several internal sidewalls. There are two parameters that affect the properties of the



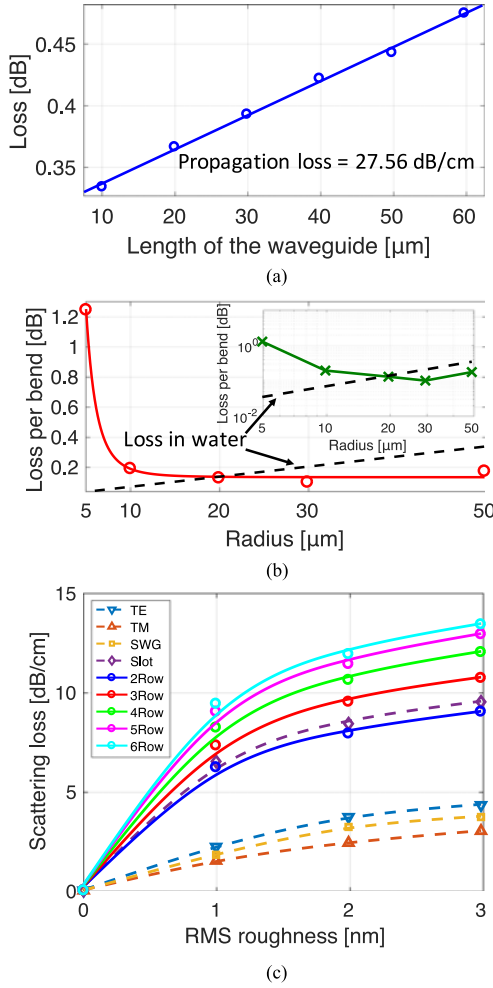


Fig. 3. (a) Simulated propagation loss of the 5-row multi-box waveguide with a varied length at 1550 nm in the TE mode ( $t = 220$  nm,  $\Lambda = 240$  nm and  $\eta = 75\%$ ). (b) Simulated waveguide bend loss versus radius for the 5-row multi-box waveguides in dB scale. Inset: Simulated waveguide bend loss versus radius in log dB scale. (c) Scattering loss of different rows multi-box waveguides ( $\Lambda = 240$  nm and  $\eta = 75\%$ ), SWG waveguides ( $\Lambda = 250$  nm and  $\eta = 70\%$ ), slot waveguides ( $w_{slot} = 60$  nm and  $w_{total} = 500$  nm) in the TE mode, and conventional strip waveguides in the TE and TM modes as a function of the RMS roughness value from 0 to 2 nm; the  $L_c$  is fixed as 50 nm.

scattering process: the correlation length ( $L_c$ ) of disorder, which is the distance between one to another correlated defect [44], and root-mean-square (RMS) roughness ( $\sigma$ ). For a typical SOI fabrication technology [45], [46],  $L_c$  is 50 nm and  $\sigma$  is less than 2 nm. To compare the influence of sidewall roughness on different waveguide geometries, 3D-FDTD simulations with Bloch boundary conditions are employed to calculate the additional loss by adding a rough surface element in the models. Fig. 3(c) presents the scattering loss in the following waveguide geometries for  $\sigma$  varied between 0 and 3 nm with a fixed 50 nm  $L_c$ ; a) 2 to 6-row multi-box waveguides with  $\Lambda = 240$  nm and  $\eta = 75\%$ , b) SWG waveguides with  $\Lambda = 250$  nm and  $\eta = 70\%$ , c) slot waveguides with a slot width of  $w_{slot} = 60$  nm in the TE mode, and d) conventional strip waveguides in the TE and TM modes. Scattering losses in multi-box waveguides are found to be much higher than in conventional strip and SWG waveguides. For 5-row multi-box waveguides, the scattering loss is roughly

11.4 dB/cm with  $\sigma = 2$  nm. Thus, additional loss introduced by fabrication has a significant impact on multi-box waveguides.

Several efforts have been made to minimize the losses caused by bend radiation or material absorption, which can also be applied to the multi-box microring resonator biosensor for further improvement. By introducing the trapezoidal silicon pillars as building blocks of the SWG microring resonator, the bend loss can be significantly reduced by using an asymmetric effective index profile, and therefore the quality factor of a microring resonator can be improved [47]. Another approach is to replace the wavelength of the light source from 1550 nm to 1310 nm, where the water absorption has been observed to be roughly 10 times lower [48].

### C. Temperature Stability

The waveguide's thermo-optic coefficient ( $TOC$ ) is dependent on the materials, so different ratios of cladding to Si in the waveguide will influence the temperature sensitivity of the device. With the material's  $TOC$ s given for silicon, silicon oxide and water ( $TOC_{SiO_2} = 2.8 \times 10^{-5}/K$  [5],  $TOC_{Si} = 1.87 \times 10^{-4}/K$  [5], and  $TOC_{H_2O} = -9.9 \times 10^{-5}/K$  [49]), the refractive index of the water cladding decreases when the environment temperature rises, which is opposite to silicon and silicon oxide. As a result, the thermal-based change of the effective index with water cladding is smaller as compared with the oxide cladding, and leads a reduced temperature sensitivity. Conventional strip waveguides are the most temperature sensitive structures due to the high Si percentage and strong confinement in the cross-section. With the decrease of the Si proportion in the core waveguide from strip to SWG, more light propagates in the cladding layer which effectively minimizes the shift of resonance wavelengths. Therefore, it is possible to design a thermally independent waveguide geometry with water cladding if the portion of water and Si in the waveguide is fine-tuned.

### D. Sensitivity and Detection Limit

There are several objective metrics that can be used for evaluating the sensing performance such as: bulk sensitivity ( $S_b$ ), surface sensitivity ( $S_s$ ), quality factor ( $Q$ ), and the limit of detection ( $LoD$ ).

Two types of sensitivity are important to silicon photonic microring resonators in biosensing applications. The first one is bulk RI sensitivity ( $S_b$ ), which takes into account refractive index changes of the waveguide's entire cladding [50]:

$$S_b = \frac{\Delta\lambda_{res}}{\Delta n_{clad}} = \frac{\lambda_{res}}{n_g} \left( \frac{\partial n_{eff}}{\partial n_{clad}} \right) \quad (1)$$

where  $\lambda_{res}$  is the sensor's resonant wavelength, and  $n_{clad}$  is the cladding's refractive index unit (RIU). Bulk sensitivity is defined as the change in resonance wavelength ( $\Delta\lambda_{res}$ ) caused by per change in refractive index unit ( $\Delta n_{clad}$ ) of the cladding above the device. Surface RI sensitivity ( $S_s$ ) assesses wavelength shifts per refractive index change within the first few tens

of nanometers (adlayer thickness) on the waveguide:

$$S_s = \frac{\Delta\lambda_{res}}{\Delta t_{ad}} = \frac{\lambda_{res}}{n_g} \left( \frac{\partial n_{eff}}{\partial t_{ad}} \right) \quad (2)$$

where  $t_{ad}$  is the uniform thickness of the adsorbed molecule layer with refractive index  $n_{ad}$ . For most proteins, the refractive index is about  $n_{ad} = 1.48$ . Surface sensitivity is used to detect the change in resonance wavelength ( $\Delta\lambda_{res}$ ) resulting from the change of the adlayer thickness which can change the refractive index above the device. As a biosensor, surface sensitivity is a more valuable metric in target molecule detection.

The quality factor is used to measure the photon lifetime in the resonator and represent the number of oscillations before the optical field intensity has decayed to 37% ( $1/e$ ).  $Q$  incorporates the total loss of a resonator and is approximated by dividing the resonant peak's wavelength ( $\lambda_{res}$ ) by its full width at half maximum (FWHM) [50]:

$$Q = \omega_{res} \frac{\varepsilon}{\partial\varepsilon/\partial t} = \frac{2\pi \cdot n_g \cdot 4.34}{\lambda_{res} \cdot \alpha_{(dB/m)}} \approx \frac{\lambda_{res}}{\Delta\lambda_{FWHM}} \quad (3)$$

where  $\alpha$  is the losses in the resonator,  $\omega_{res} = 2\pi f_{res}$  is the resonance frequency,  $\partial\varepsilon/\partial t$  is the mode's energy versus time,  $n_g$  is the group index, and  $\Delta\lambda_{FWHM}$  is the FWHM bandwidth of the resonance peak.

The system's limit of detection ( $sLoD$ ) is defined as the minimum refractive index change or mass change to cause a detectable change in the output signal. As the  $sLoD$  depends on the readout instrumentation and the experimental setup, it is challenging to have an objective comparison between sensors characterized using different assays and experimental systems. To solve the comparison problem, the intrinsic limit of detection ( $iLoD$ ) was introduced as a substitute [51]:

$$iLoD = \frac{\lambda_{res}}{Q \cdot S} \quad (4)$$

where  $\lambda_{res}$  is the sensor's resonant wavelength,  $Q$  is the quality factor of the resonator, and  $S$  is the sensitivity. The  $iLoD$  can be translated as the smallest index change required to shift the resonance wavelength by one line-width.

For multi-box waveguides, the sensing performance is greatly enhanced by a weak mode confinement and a highly condensed electric field in the gaps [as shown in Fig. 2(b)], both of which increase the modal overlap with the analyte. Therefore, a proper simulation is needed for the 5-row multi-box microring resonator's sensitivity analysis. There are two approaches usually selected for the simulation of periodic sub-wavelength structures: 2D simulation with the equivalent effective waveguide model, and 3D simulation with the Bloch boundary conditions [28], which can offer more precise results. Fig. 4 shows the 3D simulation results using Lumerical FDTD Solutions. As a comparison, we selected a strip waveguide ( $w = 750$  nm,  $t = 220$  nm) for the TM polarized mode [32], an SWG waveguide ( $w = 500$  nm,  $t = 220$  nm,  $\Lambda = 250$  nm,  $\eta = 70\%$ ) [28], and a multi-box waveguide with five rows ( $w = 1200$  nm,  $t = 220$  nm,  $\Lambda = 240$  nm and  $\eta = 75\%$ ) for the TE polarized mode to characterize the bulk and surface sensitivities. The bulk sensitivities are approximately 600 nm/RIU for the multi-box waveguide,

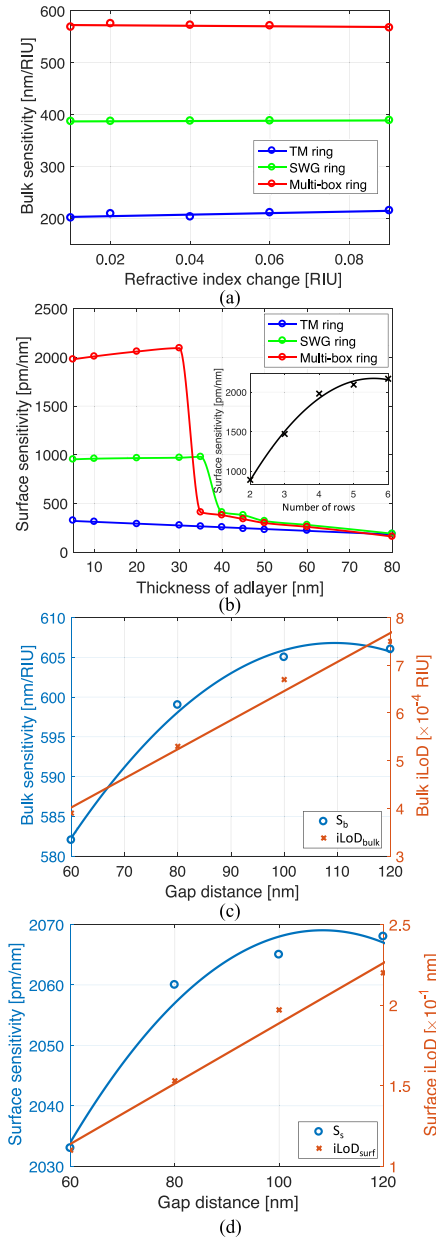


Fig. 4. (a) Comparison of the curve-fitted simulation results by FDTD Solutions on the bulk and (b) surface sensitivities for different waveguide geometries: the TM mode strip waveguide ( $w = 750$  nm,  $t = 220$  nm), SWG waveguide ( $w = 500$  nm,  $t = 220$  nm,  $\Lambda = 250$  nm,  $\eta = 70\%$ ) and 5-row multi-box waveguide ( $w = 1200$  nm,  $t = 220$  nm,  $\Lambda = 240$  nm and  $\eta = 75\%$ ) in the TE mode, respectively. Inset: The surface sensitivity as a function of the number of rows of multi-box waveguides. (c) The relationships of the simulated bulk sensitivity and the  $iLoD_{bulk}$ , and (d) the simulated surface sensitivity and the  $iLoD_{surf}$  of the 5-row multi-box waveguide with different gap distances in the propagation direction after fitting calculations.

400 nm/RIU for the SWG waveguide in the TE mode, and 200 nm/RIU for the TM mode waveguide in Fig. 4(a).

As for the surface sensitivity, the evanescent field intensity drops with the increase of the surface adlayer thickness, ranging from a few to tens of nanometers, which results in a considerable drop of the surface sensitivity before reaching the final target to be detected [28], [29]. To compare the thickness dependency, a precise 3D simulation is applied to demonstrate the

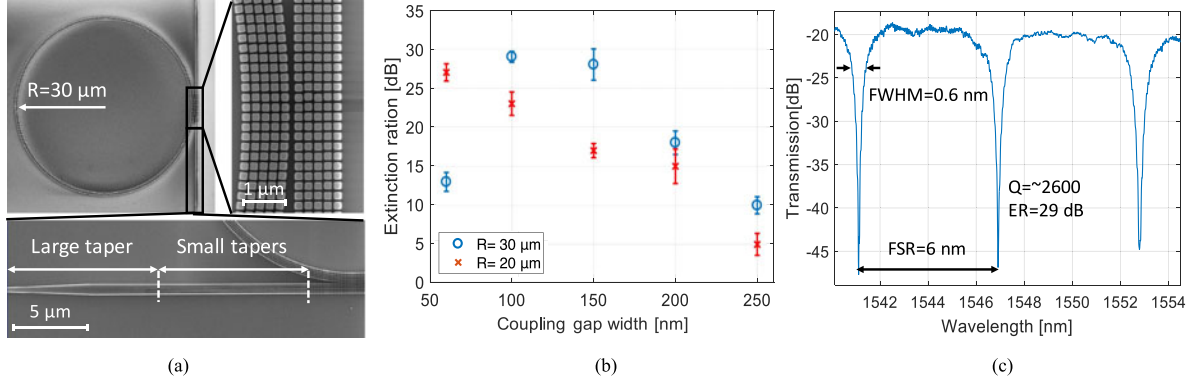


Fig. 5. (a) SEM images of the multi-box microring resonator ( $R = 30 \mu\text{m}$ ,  $w = 1200 \text{ nm}$ ,  $t = 220 \text{ nm}$ ,  $\Lambda = 240 \text{ nm}$  and  $\eta = 75\%$ ) with five rows fabricated by the EBL. (b) The measured  $ER$  values of the multi-box microrings with the coupling gap widths from 60 nm to 250 nm. (c) Measured transmission spectrum of the fabricated multi-box microring resonator with  $FSR = 6 \text{ nm}$ ,  $Q = \sim 2600$  and  $ER = 29 \text{ dB}$ .

surface sensitivity of each structure with varied thicknesses of well-distributed protein adlayers. For a surface with optimum occupation by proteins, the refractive index would be  $n_{ad} = 1.48$ . The surface sensitivities in multi-box and SWG waveguides are significantly improved compared to that in a conventional strip waveguide in the TM mode [as shown in Fig. 4(b)], which is due to the higher mode overlap. Moreover, these values remain constantly high for the adlayer thickness below 30 nm and 35 nm for multi-box and SWG waveguides. A sharp reduction of sensitivities is observed then, since the gaps between the Si segments have been already filled up, and only the top layer increases, which is consistent with previous researchers' results: the confined field between silicon segments extends the surface sensing region, but the surface sensitivity becomes insensitive to the surface layer thickness [29]. The maximum surface sensitivities presented in Fig. 4(b) are roughly 2000 pm/nm, 1000 pm/nm and 300 pm/nm for the multi-box, SWG waveguides in the TE mode, and the TM mode strip waveguide respectively. In addition, we also demonstrate the surface sensitivity as a function of the number of rows of multi-box waveguides in the inset of Fig. 4(b). The sensitivity stops the obvious growth trend after the number of rows reaches 4. Although both 5-row and 6-row multi-box waveguides show substrate-loss-negligible effective indices in Fig. 2(a), adding more rows in a multi-box waveguide may further increase the water absorption and multi-sidewall roughness loss as in Fig. 3(c).

Fig. 4(c) and (d) present the simulation results of sensitivity and  $iLoD$  values of the five-row multi-box structure with different gap distances = 60, 80, 100 and 120 nm in the propagation direction. Since the portion of Si is reduced accordingly to the gap distance increase when the  $180 \times 180 \text{ nm}^2$  Si square is confirmed, the effective index of the five-row multi-box waveguide will decrease. This impacts the sensitivity and the quality factor directly: lower effective index gives rise to a weaker optical confinement, which increases both the sensitivity and the loss. It is observed from Fig. 4(c) and (d) that the best (lowest)  $iLoD$  values are achieved when the gap is 60 nm ( $iLoD_{bulk} = 3.9 \times 10^{-4} \text{ RIU}$  and  $iLoD_{surf} = 1.1 \times 10^{-1} \text{ nm}$ ), which is caused by the lower simulated  $Q$  values with larger gaps (6800, 4900, 3800 and 3400 for the gap distances of 60, 80, 100 and 120 nm).

Furthermore, according to the study from Collaud Coen *et al.*, the thickness of the 2-layer protein A and IgG is between 8 and 13.5 nm, in which the IgG itself has a height of 8.5 nm [52]. It indicates that 60 nm gap distance (30 nm for each sidewall of the hole) is wide enough for a standard bio-sandwich assay since the total thickness is mainly generated by the IgG, the largest protein in the assay. As a result, a 60 nm gap distance, which is also the minimum feature size of our fabrication, is chosen as the segmentation for each Si box.

### III. EXPERIMENTS AND RESULTS

#### A. Design and Fabrication

All the multi-box devices were realized on an SOI wafer with a 220 nm thick top silicon layer and a  $2 \mu\text{m}$  thick BOX layer using the NanoSOI MPW fabrication process by Applied Nanotools Inc. (Edmonton, Canada). The device pattern is defined by direct-write 100 keV electron-beam lithography (EBL) and transferred into the underlying silicon layer by an anisotropic inductively coupled plasma reactive-ion etching (ICP-RIE) process [38]. Multi-box microrings with radii of 20 and  $30 \mu\text{m}$ , and coupling gaps  $g = 60, 100, 150, 200$  and  $250 \text{ nm}$  were fabricated and characterized to determine the optimal extinction ratio ( $ER$ ) and  $Q$  values. To minimize the mode mismatch loss, a circular shape is selected for the multi-box microring resonator as opposed to a racetrack resonator to eliminate the straight to bent mode mismatch losses,  $10 \mu\text{m}$  long tapers are used to transform from a  $500 \text{ nm}$  wide strip waveguide to a  $1200 \text{ nm}$  wide 5-row multi-box waveguide smoothly. Fig. 5(a) shows the scanning electron microscope (SEM) images of a 5-row multi-box microring resonator with the following waveguide geometry: microring radius  $R = 30 \mu\text{m}$ , waveguide width  $w = 1200 \text{ nm}$ , waveguide thickness  $t = 220 \text{ nm}$ , grating period  $\Lambda = 240 \text{ nm}$ , and duty cycle  $\eta = 75\%$ . The  $ER$  values of each resonator are presented in Fig. 5(b). The highest  $ER$  is obtained with a coupling gap width of 120 nm for  $30 \mu\text{m}$  microrings, whereas, for  $20 \mu\text{m}$  microrings, the gap width should be further decreased to achieve critical coupling. Although the best-measured  $ER$ s for 20 and  $30 \mu\text{m}$  microrings are similar ( $ER = \sim 30 \text{ dB}$ ), the  $Q$  decreases significantly for  $20 \mu\text{m}$  microrings due to the high



radiation loss ( $Q_{20} = \sim 1700$ ). Fig. 5(c) presents the measured transmission spectrum of the proposed multi-box microring resonator from Fig. 5(a) after the calibration to remove the insertion loss of the grating couplers. The free spectral range ( $FSR$ ) is measured to be 6 nm, corresponding to the group index calculation  $n_g = \lambda^2 / (2\pi R \cdot FSR) = 2.12$  [29]; it is close to the simulation result at 1550 nm wavelength ( $n_g = 2.15$ ), with an obtained  $Q$  of around 2600.

Multi-box microring resonators show a lower quality factor compared to strip waveguide microring resonators ( $Q = \sim 15 \times 10^3$  [31]), which means a higher attenuation in the cavity. The primary loss of silicon photonic sensors is due to the water absorption at 1550 nm wavelengths. However, multi-box devices have an increased portion of light propagating in the gaps, which enhances their susceptibility to the cladding material absorption and sidewall roughness scattering. If we only consider the water absorption, we can obtain a fundamental limit on the intrinsic  $Q$  for specific resonators based on Equation 3. According to the simulated group index ( $n_g = 2.15$ ) and the attenuation ( $\alpha_{water} = 27$  dB/cm) of the 5-row multi-box waveguides at 1550 nm wavelength by 3D FDTD, the fundamental limit of the intrinsic  $Q$  is  $14 \times 10^3$ . In the critical coupling case where the coupled power equals the power lost in the resonator, the observed  $Q$  is half the intrinsic  $Q$  [53]. Therefore, the limit for the 5-row multi-box microring resonator is  $7 \times 10^3$ , approximately 2.7X higher than the experimentally measured result. We hypothesize that the discrepancy is caused by the additional scattering loss due to the multi-sidewall roughness, as described in Fig. 3(c).

### B. Experimental Setup

Our devices were measured and characterized by using a custom silicon photonic test setup and software developed by our research group for biosensing applications [1], [28], [32], [54]. Briefly, the optical test setup consists of a tunable off-chip laser source (Agilent 81682A, with a range from 1460 to 1580 nm) with power meters (Agilent 81635A) as the detector; an optical fiber array (PLC Connections, Columbus, OH) with four polarization maintaining fibers to couple the light on and off the chip; a thermally tuned aluminum stage controlled by a temperature controller (SRS LDC501); a poly(methyl methacrylate) (PMMA)/polydimethylsiloxane (PDMS) gasket with 2 parallel 300- $\mu$ m-wide channels over the optical sensor and a syringe pump (Chemiyx Nexus 3000) to sequence the reagents through the channels [Fig. 6(a)]. All the instruments are controlled by a Windows PC.

For the refractive index measurement process, a small  $FSR$  can limit the dynamic range. We can solve this issue by performing repeated wavelength scans (25 seconds per scan) and using a peak-finding routine to identify the peak even if it shifts by more than the  $FSR$  of the resonator.

### C. Temperature Sensitivity

We characterize the temperature sensitivity of three different waveguide geometries based microring resonators with the same radius of 30  $\mu$ m; 1) the TM mode strip waveguide ( $w = 750$  nm,  $t = 220$  nm), 2) SWG ( $w = 500$  nm,  $t = 220$  nm,

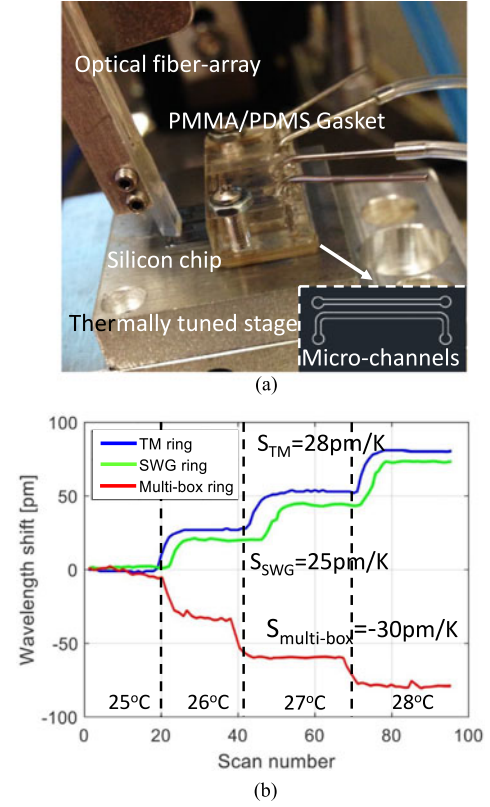


Fig. 6. (a) Custom silicon photonics biosensing measurement setup. Inset: Parallel microfluidic channels on the PDMS layer of gasket. (b) Resonant wavelength shifts caused by different temperatures of three resonators: the TM mode microring ( $w = 750$  nm,  $t = 220$  nm), SWG microring ( $w = 500$  nm,  $t = 220$  nm,  $\Lambda = 250$  nm,  $\eta = 70\%$ ) and 5-row multi-box microring ( $w = 1200$  nm,  $t = 220$  nm,  $\Lambda = 240$  nm and  $\eta = 75\%$ ) in the TE mode.

$\Lambda = 250$  nm,  $\eta = 70\%$ ) and 3) 5-row multi-box ( $w = 1200$  nm,  $t = 220$  nm,  $\Lambda = 240$  nm and  $\eta = 75\%$ ) microring resonators in the TE mode. The temperature of the stage is controlled by the thermal controller and ranged from 25 to 28  $^{\circ}$ C during the injection of DI water above the devices. The flow rate is regulated at 1  $\mu$ L/min to minimize the temperature difference between the waveguides and water cladding. Fig. 6(b) presents the resonant wavelength shifts of the three resonators for different temperatures. Due to the lowest Si ratio in the waveguide core, the multi-box microring resonator shows a blue shift when increasing the temperature ( $S_{multi-box} = -30$  pm/K), whereas for the TM mode and SWG resonators, red shifts were observed ( $S_{TM} = 28$  pm/K and  $S_{SWG} = 25$  pm/K).

### D. Bulk RI Sensitivity

A set of IPA (JT Baker, 4L) with different concentrations ranging from 5% to 20% (v/v) were selected as the refractive index standards for bulk sensitivity measurements. Since IPA is soluble in water and volatile at room temperature, no residues are left on the silicon chip after rinsing and drying by nitrogen. Just like the previous experiments, the 750 nm wide TM mode strip waveguide and SWG waveguide based microring resonators were measured for comparison to characterize the sensing performance of the multi-box microring resonator.

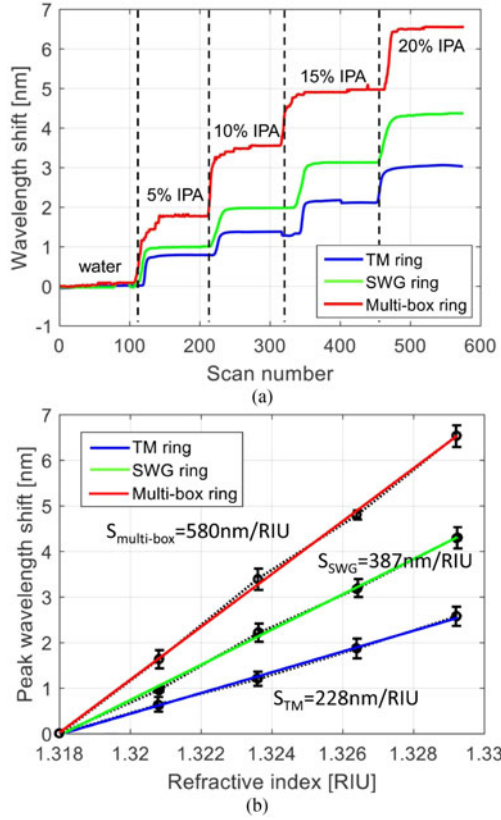


Fig. 7. (a) Measured peak wavelength shifts of three resonators: the TM mode microring ( $w = 750 \text{ nm}$ ,  $t = 220 \text{ nm}$ ), SWG microring ( $w = 500 \text{ nm}$ ,  $t = 220 \text{ nm}$ ,  $\Lambda = 250 \text{ nm}$ ,  $\eta = 70\%$ ) and 5-row multi-box microring ( $w = 1200 \text{ nm}$ ,  $t = 220 \text{ nm}$ ,  $\Lambda = 240 \text{ nm}$  and  $\eta = 75\%$ ) in the TE mode. (b) Calculated bulk sensitivity results of each resonator at  $25^\circ\text{C}$ .

The stage is thermally tuned to  $25^\circ\text{C}$  during the optical measurement to minimize the impact of external thermal noise and drift. Each sensor was measured multiple times for each concentration to ensure the stability and accuracy of the signal. Fig. 7(a) shows the steps of resonant wavelength shifts on three different microring structures. The slopes of the wavelength shift per change of RI provide the bulk sensitivities, which are  $S_{TM} = 228 \text{ nm/RIU}$ ,  $S_{SWG} = 387 \text{ nm/RIU}$  and  $S_{multi-box} = 580 \text{ nm/RIU}$  respectively [Fig. 7(b)]. According to the measured  $Q$  in Fig. 5(c) and  $S_{multi-box}$ , we can achieve an  $iLoD_{bulk}$  of  $1.02 \times 10^{-3} \text{ RIU}$  for the multi-box microring resonator. Similarly, based on the measured  $Q$  values of the  $750 \text{ nm}$  TM mode and SWG waveguides based resonators ( $Q_{TM} = 10778$ ,  $Q_{SWG} = 5270$ ), we also calculated bulk  $iLoD$  values of  $6.3 \times 10^{-4} \text{ RIU}$  and  $7.6 \times 10^{-4} \text{ RIU}$  respectively.

### E. Demonstration for Biosensing

The biosensing performance of the multi-box microring resonators was evaluated by using a standard sandwich assay to probe biomolecular interactions with specific and non-specific targets. As illustrated in Fig. 8(a), the sensor was rinsed with PBS buffer ( $\text{pH} = 7.39$ ,  $n = 1.35$ ) for 20 minutes to achieve a baseline at  $37^\circ\text{C}$  before any functionalization. Protein A ( $0.5 \text{ mg/mL}$ ,  $\text{MW} \sim 42 \text{ kDa}$ , ThermoFisher, Chicago, IL), a

globular protein with a diameter of  $3 \text{ nm}$  [55] and a refractive index of  $1.48$  [56], was first introduced to the sensor's surface for irreversible binding as shown in Region A. This process has been proven to facilitate the immobilization and orientation of the capture antibodies [57], [58]. After passive adsorption of Protein A, the capture antibody, anti-Streptavidin (antiSA,  $20 \mu\text{g/mL}$ ,  $\text{MW} \sim 150 \text{ kDa}$ , Vector Labs, Burlingame, CA) was introduced and bound to the Protein A adlayer for sensor functionalization (Region B). Then, to prevent unwanted adsorption to the sensor's surface, Bovine Serum Albumin (BSA,  $30 \mu\text{g/mL}$ ,  $\text{MW} \sim 66 \text{ kDa}$ ) was introduced to block any remaining exposed surface sites, as shown in Region C. Next, the functionalized and blocked sensor was subjected to Streptavidin (SA,  $20 \mu\text{g/mL}$ ,  $\text{MW} \sim 57 \text{ kDa}$ , Vector Labs, Burlingame, CA) presented in Region D, which can be bound by the antibody specifically and irreversibly. In the final step, biotin conjugated with BSA ( $50 \mu\text{g/mL}$ ,  $\text{MW} \sim 66 \text{ kDa}$ , Vector Labs, Burlingame, CA) was introduced as an amplification step, and since biotin and SA have one of the strongest non-covalent binding interactions [59], another permanent resonant shift could be observed in Region E. Each reagent was followed by a 30 min PBS buffer rinse to remove any unbound molecule on the sensor's surface [blue area labeled 'PBS' in Fig. 8(b)] when they were injected over the sensor sequentially.

Fig. 8(b) shows the peak wavelength shifts of the biological sandwich assay on three different microring resonator devices; TM mode, SWG and 5-row multi-box. Comparing with the TM and SWG microring resonators, the multi-box waveguide-based sensor shows a great enhancement in each wavelength shift caused by different protein layers added on the surface. It is reported that Protein A can form a physisorbed layer of approximately  $1\text{--}3 \text{ nm}$  thick [54], [58]. However, in reality, the surface coverage of the protein adlayer is not  $100\%$ ; a constant refractive index of the protein layer ( $n_{protein} = 1.48$ ) with changing effective thickness is selected as a thin layer simulation. Assuming this variation is linear [56], our simulation indicates that a  $1 \text{ nm}$  layer needs to cover  $42\%$  of the sensor's surface to result in the observed wavelength shift for the multi-box device in Region A. Likewise, a  $3 \text{ nm}$  layer needs to cover  $14\%$  of the surface to lead to a similar wavelength shift. If an antibody can be modeled as a  $5 \text{ nm}$  diameter cylinder with  $10 \text{ nm}$  height [28], the shifts in Region B suggest a  $1.4 \text{ nm}$  uniform adlayer, or approximately  $14\%$  surface coverage, which is also well agreed with the previous surface coverage values for antibodies [28], [54], [58]. There is no obvious shift in Region C, which may be due to the surface saturation after introducing the antibody resulting in no potential sites for further binding of BSA. In Region D and E, the wavelength shift of Biotin-BSA is approximately  $2X$  higher than the shift of SA, which indicates that not all four binding sites are occupied with Biotin-BSA, although SA is tetravalent. There is a slight tilt observed in peak-shift curves which represents a slow blueshift happening simultaneously during the assay. This phenomenon has been reported and interpreted as the Si oxidation by water [60]. The total thickness of captured protein multi-layers is estimated to be around  $15$  to  $30 \text{ nm}$  [54]; considering the situation of  $14\%$  surface coverage, the effective thickness is between  $2.1$  to  $4.2 \text{ nm}$ . Based on the overall



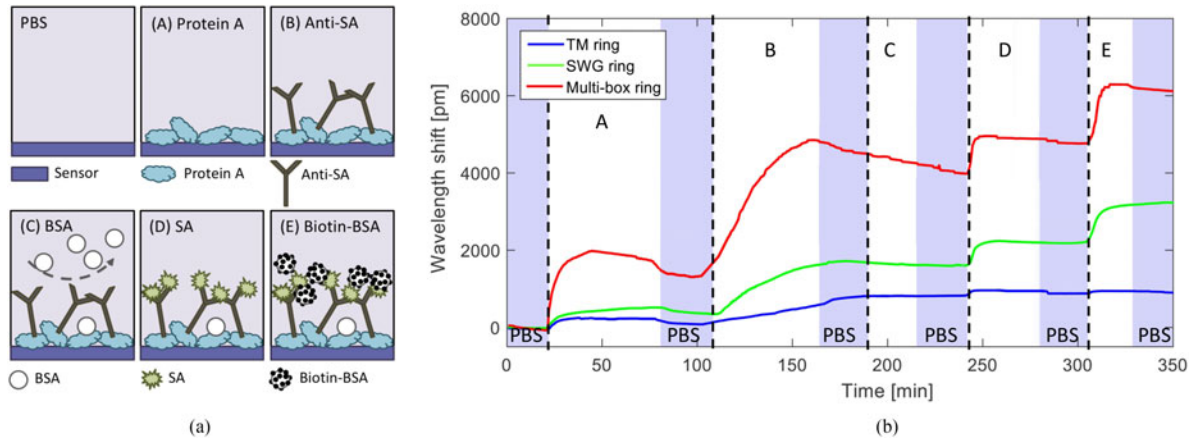


Fig. 8. (a) Schematic of standard biological sandwich bioassay: Region A = Protein A (0.5 mg/mL), B = anti-streptavidin (antiSA) (20  $\mu$ g/mL), C = Bovine Serum Albumin (BSA) (30  $\mu$ g/mL), D = streptavidin (SA) (20  $\mu$ g/mL), and E = biotinylated-BSA (50  $\mu$ g/mL). The model is not in scale. (b) Real-time biosensing experimental results of the resonance shift for the TM ( $w = 750$  nm,  $t = 220$  nm), SWG ( $w = 500$  nm,  $t = 220$  nm,  $\Lambda = 250$  nm,  $\eta = 70\%$ ) and multi-box ( $w = 1200$  nm,  $t = 220$  nm,  $\Lambda = 240$  nm and  $\eta = 75\%$ ) microring resonators during the bio-sandwich assay. The sensor is washed with PBS for 30 min after each reagent presented in blue area.

wavelength shifts presented in Fig. 8(b) ( $\Delta\lambda_{\text{multi-box}} = 6000$  pm,  $\Delta\lambda_{\text{SWG}} = 3000$  pm and  $\Delta\lambda_{\text{TM}} = 1000$  pm), surface sensitivities of 1900, 950 and 310 pm/nm are observed for the multi-box, SWG and TM microring resonators, which agree well with the simulation results in Fig. 4(b). We can further obtain the values of surface  $iLoD$  of the three measured structures, which are  $3.13 \times 10^{-1}$  nm for multi-box,  $3.26 \times 10^{-1}$  nm for SWG, and  $4.64 \times 10^{-1}$  nm for TM microring resonators.

#### IV. CONCLUSION

In conclusion, we have demonstrated a highly sensitive silicon photonic biosensor by using a sub-wavelength multi-box microring resonator, resulting in 1.5X and 2X improvement in bulk and surface sensitivities compared to the SWG microring resonators recently reported. The simulated and experimental results indicate that the optical power is largely congregated in the gaps between the Si segments which greatly enhances the overlap between the evanescent field and analyte. However, there are challenges with this approach. First, although the sensitivity is significantly improved, the bulk  $iLoD$  of  $1.02 \times 10^{-3}$  RIU and surface  $iLoD$  of  $3.13 \times 10^{-1}$  nm are comparable to other SWG and other silicon based sensors as a result of the relatively low measured  $Q$  value of 2600 in water. Second, the manufacture of sub-wavelength structures requires either the EBL system, or the most advanced 193 nm immersion lithography technology (demonstrated silicon photonics features down to 50 nm [61]). Further work will focus on minimizing the scattering loss in multi-box waveguides by applying the new advanced fracturing strategies, single line edge smoothing (SLS), in EBL [62], and optimizing the waveguide structure for thermally-independent operation.

#### ACKNOWLEDGMENT

The authors also would like to thank Lumerical, Inc., for the simulation software, M. Köfferlein's KLayout for the layout tool, and Applied Nanotools, Inc., for sample fabrication.

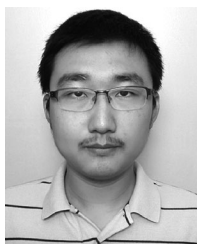
#### REFERENCES

- [1] S. Schmidt *et al.*, "Improving the performance of silicon photonic rings, disks, and Bragg gratings for use in label-free biosensing," *Proc. SPIE*, vol. 9166, Aug. 2014, Art. no. 91660M.
- [2] J. R. Crowther, *The ELISA Guidebook*. Totowa, NJ, USA: Humana Press, 2001.
- [3] G. Y. Wiederschain, *The ELISA Guidebook*. New York, NY, USA: Humana Press, 2009.
- [4] J. L. Arlett, E. B. Myers, and M. L. Roukes, "Comparative advantages of mechanical biosensors," *Nature Nanotechnol.*, vol. 6, no. 4, pp. 203–215, 2011.
- [5] L. Chrostowski and M. Hochberg, *Silicon Photonics Design: From Devices to Systems*. Cambridge, U.K.: Cambridge Univ. Press, 2015.
- [6] A. Fernández Gavela, D. Grajales García, J. C. Ramirez, and L. M. Lechuga, "Last advances in silicon-based optical biosensors," *Sensors*, vol. 16, no. 3, 2016, Art. no. 285.
- [7] M. S. Luchansky, A. L. Washburn, M. S. McClellan, and R. C. Bailey, "Sensitive on-chip detection of a protein biomarker in human serum and plasma over an extended dynamic range using silicon photonic microring resonators," *Lab Chip*, vol. 11, no. 12, pp. 2042–2044, 2011.
- [8] R. W. Boyd and J. E. Heebner, "Sensitive disk resonator photonic biosensor," *Appl. Opt.*, vol. 40, no. 31, pp. 5742–5747, 2001.
- [9] S. T. Fard *et al.*, "Label-free silicon photonic biosensors for use in clinical diagnostics," *Proc. SPIE*, vol. 8629, Mar. 2013, pp. 862909.
- [10] W. C. Lai, S. Chakravarty, Y. Zou, Y. Guo, and R. T. Chen, "Slow light enhanced sensitivity of resonance modes in photonic crystal biosensors," *Appl. Phys. Lett.*, vol. 102, no. 4, 2014, Art. no. 041111.
- [11] F. Liang, N. Clarke, P. Patel, M. Loncar, and Q. Quan, "Scalable photonic crystal chips for high sensitivity protein detection," *Opt. Express*, vol. 21, no. 26, pp. 32 306–32 312, 2013.
- [12] H. Yan *et al.*, "Silicon on-chip bandpass filters for the multiplexing of high sensitivity photonic crystal microcavity biosensors," *Appl. Phys. Lett.*, vol. 106, no. 12, 2015, Art. no. 121103.
- [13] Y. Zou *et al.*, "Cavity-waveguide coupling engineered high sensitivity silicon photonic crystal microcavity biosensors with high yield," *IEEE J. Sel. Topics Quantum Electron.*, vol. 20, no. 4, Jul./Aug. 2014, Art. no. 6900710.
- [14] W. Bogaerts *et al.*, "Silicon microring resonators," *Laser Photon. Rev.*, vol. 6, no. 1, pp. 47–73, 2012.
- [15] A. J. Qavi and R. C. Bailey, "Multiplexed detection and label-free quantitation of microRNAs using arrays of silicon photonic microring resonators," *Angewandte Chem. Int. Ed. Engl.*, vol. 49, no. 27, pp. 4608–4611, 2010.
- [16] F. Vollmer, S. Arnold, and D. Keng, "Single virus detection from the reactive shift of a whispering-gallery mode," *Proc. Nat. Acad. Sci.*, vol. 105, no. 52, pp. 20 701–20 704, 2008.
- [17] A. L. Washburn, L. C. Gunn, and R. C. Bailey, "Label-free quantitation of a cancer biomarker in complex media using silicon photonic microring resonators," *Anal. Chem.*, vol. 81, no. 22, pp. 9499–9506, 2008.

- [18] S. Rodriguez-Mozaz, M. J. López de Alda, M. P. Marco, and D. Barceló, "Biosensors for environmental monitoring: A global perspective," *Talanta*, vol. 65, no. 2, pp. 291–297, 2005.
- [19] W. Zhang, S. Serna, X. Le Roux, L. Vivien, and E. Cassan, "Highly sensitive refractive index sensing by fast detuning the critical coupling condition of slot waveguide ring resonators," *Opt. Lett.*, vol. 41, no. 3, pp. 532–535, 2016.
- [20] J. G. Wangüemert-Pérez *et al.*, "Evanescent field waveguide sensing with subwavelength grating structures in silicon-on-insulator," *Opt. Lett.*, vol. 39, no. 15, pp. 4442–4445, 2014.
- [21] C. F. Carlborg *et al.*, "A packaged optical slot-waveguide ring resonator sensor array for multiplex label-free assays in labs-on-chips," *Lab Chip*, vol. 10, no. 3, pp. 281–290, 2010.
- [22] T. Claes *et al.*, "Label-free biosensing with a slot-waveguide-based ring resonator in silicon on insulator," *IEEE Photon. J.*, vol. 1, no. 13, pp. 197–204, Sep. 2009.
- [23] P. Cheben, D.-X. Xu, S. Janz, and A. Densmore, "Subwavelength waveguide grating for mode conversion and light coupling in integrated optics," *Opt. Express*, vol. 14, no. 11, pp. 4695–4702, 2006.
- [24] P. J. Bock *et al.*, "Subwavelength grating periodic structures in silicon-on-insulator: A new type of microphotonic waveguide," *Opt. Express*, vol. 18, no. 19, pp. 20 251–20 262, 2010.
- [25] P. Cheben *et al.*, "Refractive index engineering with subwavelength gratings for efficient microphotonic couplers and planar waveguide multiplexers," *Opt. Lett.*, vol. 35, no. 15, pp. 2526–2528, 2010.
- [26] R. Halir *et al.*, "Waveguide sub-wavelength structures: A review of principles and applications," *Laser Photon Rev.*, vol. 9, no. 1, pp. 25–49, 2015.
- [27] R. Halir *et al.*, "Subwavelength metamaterial engineering for silicon photonics," *Smart Photon. Optoelectron. Integr. Circuits XIX*, vol. 10107, Feb. 2017, Art. no. 1010703.
- [28] J. Flueckiger *et al.*, "Sub-wavelength grating for enhanced ring resonator biosensor," *Opt. Express*, vol. 24, no. 14, pp. 15 672–15 686, 2016.
- [29] H. Yan *et al.*, "Unique surface sensing property and enhanced sensitivity in microring resonator biosensors based on subwavelength grating waveguides," *Opt. Express*, vol. 24, no. 26, pp. 29724–29733, 2016.
- [30] L. Huang *et al.*, "Improving the detection limit for on-chip photonic sensors based on subwavelength grating racetrack resonators," *Opt. Express*, vol. 25, no. 9, pp. 10527–10535, 2017.
- [31] S. T. Fard *et al.*, "Performance of ultra-thin SOI-based resonators for sensing applications," *Opt. Express*, vol. 22, no. 12, pp. 14166–14179, 2014.
- [32] S. T. Fard *et al.*, "Optimized sensitivity of silicon-on-insulator (SOI) strip waveguide resonator sensor," *Biomed. Opt. Express*, vol. 8, no. 2, pp. 500–511, 2017.
- [33] L. Zavargo-Peche, A. Ortega-Monux, J. G. Wangüemert-Perez, and I. Molina-Fernandez, "Fourier based combined techniques to design novel sub-wavelength optical integrated devices," *Progress Electromagn. Res.*, vol. 123, pp. 447–465, 2012.
- [34] P. Lalanne and J. P. Hugonin, "High-order effective-medium theory of sub-wavelength gratings in classical mounting: Application to volume holograms," *J. Opt. Soc. Amer. A*, vol. 15, no. 7, pp. 1843–1851, 1998.
- [35] J. Čtyroký, S. Helfert, and R. Pregla, "Analysis of a deep waveguide Bragg grating," *Opt. Quant. Electron.*, vol. 30, no. 5, pp. 343–358, 1998.
- [36] X. Wang *et al.*, "Precise control of the coupling coefficient through destructive interference in silicon waveguide Bragg gratings," *Opt. Lett.*, vol. 39, no. 19, pp. 5519–5522, 2014.
- [37] J. D. Sarmiento-Merenguel *et al.*, "Controlling leakage losses in sub-wavelength grating silicon metamaterial waveguides," *Opt. Lett.*, vol. 41, no. 15, pp. 3443–3446, 2016.
- [38] "NanoSOI fabrication process," Applied Nanotools, Inc., Edmonton, AB, Canada. 2016. [Online]. Available: <https://www.appliednt.com/nanosoi/>. Accessed on: Aug. 25, 2016.
- [39] Z. Weissman and I. Hendel, "Analysis of periodically segmented waveguide mode expanders," *J. Lightw. Technol.*, vol. 13, no. 10, pp. 2053–2058, Oct. 1995.
- [40] D. Melati, A. Melloni, and F. Morichetti, "Real photonic waveguides: Guiding light through imperfections," *Adv. Opt. Photon.*, vol. 6, no. 2, pp. 156–224, 2014.
- [41] R. J. Bojko *et al.*, "Electron beam lithography writing strategies for low loss, high confinement silicon optical waveguides," *J. Vac. Sci. Technol.*, vol. 29, no. 6, 2011, Art. no. 06F309.
- [42] W. Bogaerts *et al.*, "Compact wavelength-selective functions in silicon-on-insulator photonic wires," *IEEE J. Sel. Topics Quantum Electron.*, vol. 12, no. 6, pp. 1394–1401, Nov./Dec. 2006.
- [43] T. Baehr-Jones, M. Hochberg, C. Walker, and A. Scherer, "High-Q optical resonators in silicon-on-insulator-based slot waveguides," *Appl. Phys. Lett.*, vol. 86, no. 8, 2005, Art. no. 081101.
- [44] D. Marcuse, "Mode conversion caused by surface imperfections of a dielectric slab waveguide," *Bell Labs Tech. J.*, vol. 48, no. 10, pp. 2187–3215, 1969.
- [45] K. K. Lee, D. R. Lim, L. C. Kimerling, J. Shin, and F. Cerrina, "Fabrication of ultralow-loss Si/SiO<sub>2</sub> waveguides by roughness reduction," *Opt. Lett.*, vol. 26, no. 23, pp. 1888–1890, 2001.
- [46] F. Xia, L. Sekaric, and Y. Vlasov, "Ultracompact optical buffers on a silicon chip," *Nature Photon.*, vol. 1, no. 1, pp. 65–71, 2007.
- [47] Z. Wang, X. Xu, D. Fan, Y. Wang, and R. T. Chen, "High quality factor sub-wavelength grating waveguide micro-ring resonator based on trapezoidal silicon pillars," *Opt. Lett.*, vol. 41, no. 14, pp. 3375–3378, 2016.
- [48] L. Kou, D. Labrie, and P. Chylek, "Refractive indices of water and ice in the 0.65-to 2.5- $\mu$ m spectral range," *Appl. Opt.*, vol. 32, no. 19, pp. 3531–3540, 1993.
- [49] G. Abbate, U. Bernini, E. Ragozzino, and F. Somma, "The temperature dependence of the refractive index of water," *J. Phys. D, Appl. Phys.*, vol. 11, no. 8, 1978, Art. no. 1167.
- [50] L. Chrostowski *et al.*, "Silicon photonic resonator sensors and devices," *Proc. SPIE*, vol. 8236, Jan. 2012, Art. no. 823620.
- [51] T. Yoshie, L. Tang, and S.-Y. Su, "Optical microcavity: Sensing down to single molecules and atoms," *Sensors*, vol. 11, no. 2, pp. 1972–1991, 2011.
- [52] M. C. Coen *et al.*, "Adsorption and bioactivity of protein A on silicon surfaces studied by AFM and XPS," *J. Colloid Interface Sci.*, vol. 233, no. 2, pp. 180–189, 2001.
- [53] A. Yariv and P. Yeh, *Photonics: Optical Electronics in Modern Communications*. New York, NY, USA: Oxford Univ. Press, 2007.
- [54] S. M. Grist *et al.*, "Silicon photonic micro-disk resonators for label-free biosensing," *Opt. Express*, vol. 21, no. 7, pp. 7994–8006, 2013.
- [55] H. P. Erickson, "Size and shape of protein molecules at the nanometer level determined by sedimentation, gel filtration, and electron microscopy," *Biological Procedure Online*, vol. 11, no. 1, pp. 32–51, 2009.
- [56] J. Vörös, "The density and refractive index of adsorbing protein layers," *Biophys. J.*, vol. 87, no. 1, pp. 553–561, 2004.
- [57] G. Moja, I. Moraru, J. Sjöquist, and V. Ghetje, "Protein A as a molecular probe for the detection of antigen induced conformational change in Fc region of rabbit antibody," *Mol. Immunol.*, vol. 18, no. 5, pp. 373–378, 1981.
- [58] M. C. Coen *et al.*, "Adsorption and bioactivity of protein A on silicon surfaces studied by AFM and XPS," *J. Colloid Interface Sci.*, vol. 233, no. 2, pp. 180–189, 2001.
- [59] P. C. Weber, D. H. Ohlendorf, J. J. Wendoloski, and F. R. Salemme, "Structural origins of high-affinity biotin binding to Streptavidin," *Science*, vol. 243, no. 4887, pp. 85, 1989.
- [60] A. Janshoff *et al.*, "Macroporous p-Type silicon Fabry-Perot layers. Fabrication, characterization, and applications in biosensing," *J. Amer. Chem. Soc.*, vol. 120, no. 46, pp. 12108–12116, 1998.
- [61] S. K. Selvaraja *et al.*, "193 nm immersion lithography for high performance silicon photonic circuits," *Proc. SPIE*, vol. 9052, Mar. 2015, Art. no. 90520F-1.
- [62] S. Patrick, R. J. Bojko, S. J. Stammberger, E. Luan, and L. Chrostowski, "Improvement of silicon waveguide transmission by advanced e-beam lithography data fracturing strategies," *J. Vac. Sci. Technol. B, Nanotechnol. Microelectron.*, vol. 35, no. 6, 2017, Art. no. 06G504.



**Enxiao Luan** received the B.Sc. and M.Eng. degrees from the Harbin Institute of Technology, Harbin, China, in 2013 and 2015, respectively. Since 2015, he has been working toward the Ph.D. degree in biomedical engineering at the University of British Columbia, Vancouver, BC, Canada. His research interest focuses on silicon photonic biosensing techniques for medicine and environmental monitoring. His research interests include biosensors, silicon photonics, and microfluidics.



**Han Yun** received the B.A.Sc. degree in electrical and computer engineering and the M.A.Sc. degree in electrical engineering from the University of British Columbia (UBC), Vancouver, BC, Canada, in 2009 and 2013, respectively. He is currently working toward the Ph.D. degree in electrical engineering at UBC. His current research interests include silicon photonics and optoelectronics integration for optical communication and sensing applications.



**Loïc Laplatine** received the M.Eng. degree in physics engineering from the National Institute of Applied Sciences (INSA), Toulouse, France, in 2010, and the Ph.D. degree in surface plasmon resonance microscopy from the Commissariat for Atomic Energy (CEA), Grenoble, France in 2014. After the Ph.D. degree, he joined the University of British Columbia, Canada, in 2015, as a Postdoctoral Fellow. He research interest focuses on the technology transfer and system-level integration of silicon photonic biosensors for industrial

applications.



**Yonathan Dattner** received the B.Sc. degree in electrical engineering from the Technion-Institute of Technology, Haifa, Israel, and the M.Sc. degree in electrical computer engineering from the University of Calgary, Calgary, AB, Canada, in 2012, and was an External Student with the University of British Columbia's Microsystems and Nanotechnology Group. As the Founder and President of Luxmux Technology Corporation, he has negotiated and secured capital from private, industrial, and multiple government sources. In 2015, Luxmux received the

ASTECH award for outstanding Science and Technology Start-Up. Prior to founding Luxmux, he was with Freescale Semiconductors and helped develop its IMX application processors. In 2012, Freescale sold more than \$2 billion worth of IMX products, seen today in leading end products such as the Amazon Kindle 3, Sony PRS-650, and Kobo. He is an award-winning Entrepreneur, who has a track record of successfully commercializing innovative new technologies within the Photonics Industry. Among his awards, he was the recipient of the Queen Elizabeth II Award and the Alexander Graham Bell Canada Award through the National Science and Engineering Council of Canada. He is a Professional Member of the Association of Professional Engineers and Geoscientists of Alberta.



**Daniel M. Ratner** received the B.A. degree in chemistry from Pomona College, Claremont, CA, USA, and the Ph.D. degree in chemistry from the Massachusetts Institute of Technology, Cambridge, MA, USA, in 1999 and 2004, respectively. He is currently an Assistant Professor with the Department of Bioengineering, University of Washington, Seattle, WA, USA. As an Investigator with NESAC/BIO, his research focuses on developing biophysical tools to study glycan-dependent interactions at the surface of cells, tissues, and biomaterials. By studying carbohydrate microarray surface chemistries, he aims to unravel the roles played by cell surface carbohydrates and glycoconjugates in biological systems. His research interests include surface-modification/characterization, carbohydrate microarrays, label-free biosensors, silicon photonics, glycotecnology, global health, drug development/delivery, and host-pathogen interactions.

by cell surface carbohydrates and glycoconjugates in biological systems. His research interests include surface-modification/characterization, carbohydrate microarrays, label-free biosensors, silicon photonics, glycotecnology, global health, drug development/delivery, and host-pathogen interactions.



**Karen C. Cheung** received the B.S. and Ph.D. degrees in bioengineering from the University of California, Berkeley, CA, USA, in 1998 and 2002, respectively. From 2002 to 2005, she was a Postdoctoral Researcher with the Ecole Polytechnique Fédérale de Lausanne, Lausanne, Switzerland. She is currently with the University of British Columbia, Vancouver, BC, Canada. Her research interests include lab-on-a-chip systems for cell culture and characterization, inkjet printing for tissue engineering, and implantable neural interfaces.



**Lukas Chrostowski** (S'95–M'04–SM'16) received the B.Eng. degree in electrical engineering from McGill University, Montreal, QC, Canada, in 1998, and the Ph.D. degree in electrical engineering and computer science from the University of California, Berkeley, CA, USA, in 2004. He is currently a Professor of electrical and computer engineering with the University of British Columbia, Vancouver, BC, Canada. He co-authored the book *Silicon Photonics Design*. He is the Program Director of the Silicon Electronic-Photonic Integrated Circuits Program,

Canada. His research interests include silicon photonics, optoelectronics, fabrication and test, for applications in optical communications and biophotonics. He is the recipient of the Killam Teaching Prize at the University of British Columbia in 2014, was an elected member of the IEEE Photonics 2014–2016 Society Board of Governors, and was the recipient of a Natural Sciences and Engineering Research Council of Canada Discovery Accelerator Supplements Award in 2015.